Computation of Viscous Transonic Flow over Porous Airfoils

Chung-Lung Chen* and Chuen-Yen Chow†
University of Colorado, Boulder, Colorado
and
William R. Van Dalsem‡ and Terry L. Holst§
NASA Ames Research Center, Moffett Field, California

The viscous effects on transonic flow past an airfoil that contains a shallow cavity beneath a porous surface are studied numerically. The porous region occupies a small portion of the total airfoil surface and is located near the shock. Both an interactive boundary-layer (IBL) algorithm and a thin-layer Navier-Stokes (TLNS) algorithm have been modified for use in studying the outer flow, whereas a stream-function formulation has been used to model the inner flow in the small cavity. The coupling procedure at the porous surface is based on Darcy's law and on the assumption of a constant total pressure in the cavity. In addition, a modified Baldwin-Lomax turbulence model is used to consider the transpired turbulent bounday layer in the TLNS approach, and the Cebeci-Smith turbulence model is used in the IBL approach. According to the present analysis, a porous surface can reduce the wave drag appreciably, but it can also increase viscous losses. As has been observed experimentally in nonlifting airfoils, the numerical results indicate that the total drag may be reduced at higher Mach numbers and increased at lower Mach numbers. Furthermore, the streamline patterns of passive-shock and boundary-layer interaction are revealed in this study.

Introduction

THE transonic flow past an airfoil in flight at a high-subsonic Mach number is characterized by a shock wave standing on the upper surface. The pressure gradient of a strong shock can induce boundary-layer separation, which may increase form drag and reduce lift. On the other hand, the boundary-layer separation will reduce the shock strength and prevent the downstream movement of the shock, so that the wave drag may be reduced. Therefore, even though shock-induced separation is generally undesirable, a controlled shock-induced separation still could be used to reduce wave drag.

Boundary-layer separation and shock-wave strength may be controlled by applying appropriate blowing or suction at the airfoil surface. Appropriate blowing in the supersonic region ahead of a strong shock may cause the shock to degenerate into a series of weaker waves or to generate another oblique shock upstream of the injection region, thus resulting in a smaller pressure gradient and a smaller entropy change. The additional kinetic energy supplied by blowing would increase the mixing rate in the boundary layer and act to prevent flow separation. However, strong blowing not only thickens the boundary layer, but also probably provokes an early separation as a side effect. On the other hand, the application of suction in the strong adverse-pressure gradient region would possibly delay separation but might produce a stronger shock and cause a higher wave drag as a side effect. In addition, if the suction area is sufficiently limited, it is necessary to examine whether the resulting boundary layer is capable of overcoming the adverse pressure gradient downstream of the suction region. Either blowing or suction requires power; thus, an extra pump drag should be added to the total drag of the airfoil when an active control device is used.

A passive control device (Fig. 1), which provides blowing and suction without externally supplied power, is an attempt to reap the benefits of both blowing and suction without incurring their negative effects and without excessive use of space. Indeed, these expectations have been proven in the laboratory under certain conditions.[1-6] In addition, inviscid-flow computations[7,8] also indicate that a porous surface can reduce the wave drag. However, inviscid simulations cannot predict any effects of porosity on the viscous drag. In particular, when the shock and boundary-layer interaction becomes strong, the inviscid-flow analysis is not sufficient to describe the flow about an airfoil. It is the purpose of this paper to study the viscous effects in transonic flow past porous airfoils.

A numerical simulation was done by Olling and Dulikravich,[9] who approached the problem by using an interactive

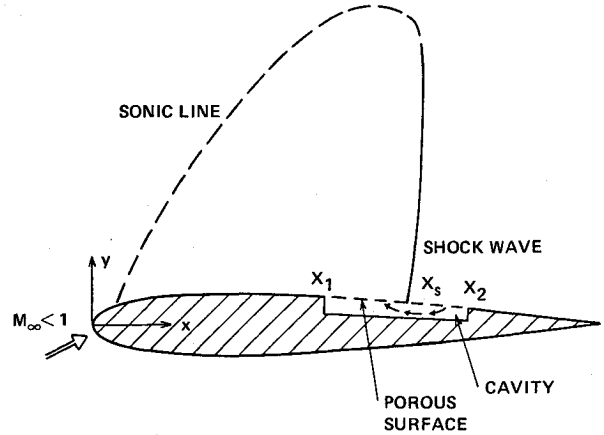

Fig. 1 Porous airfoil in transonic flow.

Presented as Paper 87-0359 at the AIAA 25th Aerospace Sciences Meeting, Reno, NV, Jan. 12-15, 1987; received March 3, 1988; revision received May 25, 1989.

*Graduate Student, currently Member of Technical Staff of Science Center, Rockwell International. Member AIAA.

†Professor, Department of Aerospace Engineering Sciences. Associate Fellow AIAA.

‡Research Scientist. Member AIAA.

§Chief, Applied Computational Fluids Branch. Associate Fellow AIAA.

boundary-layer procedure with the assumption of constant pressure in the cavity. In the present work, both interactive boundary-layer (IBL) and thin-layer Navier-Stokes (TLNS) procedures are applied separately to study the outer flow past the airfoil. In addition, the inner flow in the cavity is modeled by a stream-function formulation. The outer and inner flows are coupled at the porous surface modeled by Darcy's law.[7-9] A predictor-corrector space-marching algorithm is applied to the boundary-layer equations in the IBL procedure. The implicit approximate-factorization schemes are the main numerical algorithms for the full-potential equation in the IBL procedure, the stream-function formulation in the cavity, and the TLNS equations. The Cebeci-Smith turbulence model is used in the IBL procedure, and a modified Baldwin-Lomax turbulence model is used in the TLNS procedure.

The following presentation includes a brief description of the numerical algorithms, boundary-condition treatments, interface of outer and inner flow, turbulence models, and numerical results.

IBL Procedure

The essential components of the IBL method used in this study are a full-potential inviscid algorithm coupled with a finite-difference boundary-layer algorithm. The transonic airfoil (TAIR) full-potential code was developed by Holst[10] and Dougherty et al.[11] The present boundary-layer and viscous-inviscid interaction algorithms were developed by Van Dalsem[12] and Van Dalsem and Steger.[13] The major modifications required for this work are associated with the boundary-layer forcing function, the boundary-condition treatment, the viscous-inviscid interaction algorithm, and the turbulence model.

The inviscid transonic flow is governed by the full-potential equation. The full-potential equation written in the ξ-η computational domain is given by

$$\left(\frac{\rho U}{J}\right)_\xi + \left(\frac{\rho V}{J}\right)_\eta = 0 \tag{1a}$$

$$\rho = \left[1 - \frac{\gamma-1}{\gamma+1}(U\Phi_\xi + V\Phi_\eta)\right]^{\frac{1}{\gamma-1}} \tag{1b}$$

where

$$U = A_1\Phi_\xi + A_2\Phi_\eta \qquad V = A_2\Phi_\xi + A_3\Phi_\eta$$

$$A_1 = \xi_x^2 + \xi_y^2$$

$$A_2 = \xi_x\eta_x + \xi_y\eta_y$$

$$A_3 = \eta_x^2 + \eta_y^2$$

$$J = \xi_x\eta_y - \xi_y\eta_x$$

This equation is nondimensionalized, as outlined in Refs. 10 and 11. The variables U and V are the contravariant velocity components along the ξ and η directions, respectively. The A_1, A_2 and A_3 are metric quantities, and J is the Jacobian of the transformation. The governing equations are solved by using a fully implicit approximate-factorization scheme (AF2).[10,11] The supersonic regions are stabilized using an upwind bias of the density. Another feature of this algorithm is a consistent spatial differencing scheme that captures the freestream automatically.[14]

Viscous effects are introduced into the inviscid solver by means of a transpiration velocity $\bar{v}_n$, determined from the boundary-layer solution

$$\bar{v}_n = \frac{1}{\rho_e}\left[\frac{\partial(\rho_e u_e \delta^*)}{\partial s} + \rho_w v_n\right]$$

where v_n is the surface blowing (or suction) velocity determined from porosity effects, ρ_e and u_e are the inviscid values at the airfoil surface (or wake centerline), δ^* is the boundary-layer displacement thickness, and s is the distance along the body (or wake centerline). This equation is derived by considering the difference between the continuity equations for the inviscid and viscous flow.[9] This interaction procedure can avoid supercritical behavior and the inviscid grid generation for each iteration. Once $\bar{v}_n$ is known, the numerical boundary condition is implemented, as in Refs. 8, 12, and 13.

For the viscous flow near the airfoil surface and wakes, the nondimensionlized, nonconservative, steady, compressible boundary-layer equations are solved. These equations are written in a general $\xi(x)$, $\eta(x,y)$ coordinate system (x, y are along and normal to the body or wake centerline, respectively), as follows:

x-momentum equation:

$$\rho[u(u_\xi\xi_x + u_\eta\eta_x) + vu_\eta\eta_y] = -\beta p_\xi\xi_x + (\mu u_\eta\eta_y)_\eta\eta_y \tag{2a}$$

Energy equation:

$$\rho c_p[u(T_\xi\xi_x + T_\eta\eta_x) + vT_\eta\eta_y] = \beta u p_\xi\xi_x + (\kappa T_\eta\eta_y)_\eta + \mu(u_\eta\eta_y)^2 \tag{2b}$$

Perfect gas relation:

$$p = \rho T \tag{2c}$$

Continuity equation:

$$(\rho u)_\xi\xi_x + (\rho u)_\eta\eta_x + (\rho v)_\eta\eta_y = 0 \tag{2d}$$

These equations are nondimensionalized, as in Refs. 12 and 13. The boundary-layer equations are solved using a predictor-corrector algorithm with appropriate initial conditions.[12,13] In the present study, it was found that the viscous-inviscid interaction converges more rapidly when the ρu_ξ term in the continuity equation is treated with a central-difference operator in the blowing (and suction), as well as in the separated flow regions.

Since the boundary-layer equations are weakly coupled, they are solved in a sequential manner at each streamwise station. Overall, second-order-accurate solutions are obtained at the cost of two scalar-bidiagonal and four scalar-tridiagonal matrix inversions per streamwise station. Both direct and semi-inverse interactions are built in the code. For attached flow, pressure is specified in the direct mode. However, near and in the reversed-flow regions, in order to avoid the Goldstein singularity, the wall shear τ_w and wake-centerline velocity u_{wc} are specified in the inverse mode. By applying the x-momentum equation at the porous wall ($u_w = 0$, $v_n \neq 0$), one obtains

$$\beta p_\xi\xi_x = (\mu u_\eta\eta_y)_\eta\eta_y \,|_w - \rho v u_\eta\eta_y \,|_w \tag{3}$$

This expression allows the elimination of the $\beta p_\xi\xi_x$ term from the differenced x-momentum equation by using the following first-order finite-difference approximation:

$$\beta p_\xi\xi_x = \frac{\left(\frac{\eta_{y_2}+\eta_{y_1}}{2}\right)\left(\frac{\mu_2+\mu_1}{2}\right)\frac{u_2-u_1}{y_2-y_1} - \tau_w}{\frac{y_2-y_1}{2}} - \rho v_w\frac{\tau_w}{\mu_1} \tag{4}$$

where the subscripts 1 and 2 correspond to the wall and one grid away from the wall, respectively. Since these inverse forcing functions are cast in the general form, they can be applied to either a solid surface or a porous surface. In the inverse mode, τ_w is updated by the following viscous-inviscid interaction algorithm:

$$\tau_w^{n+1} = \tau_w^n + \omega\left(p_v^n - p_i^{n+1}\right)\xi_x \tag{5}$$

The acceleration parameter ω is gradually increased after the first few viscous-inviscid iterations, in order to isolate the viscous-inviscid scheme from high-frequency errors encountered during the early inviscid iterations. A similar procedure is used to update the wake centerline velocity. In the present work, the quantity $\omega\xi_x$ varies in a range near 10 for τ_w, and near 2 for the wake centerline velocity.

The turbulence model used in the IBL procedure is the Cebeci-Smith two-layer algebraic turbulence model. Cebeci and Smith extended Van Driest's modeling of the viscous sublayer and let A^+ be a function of v^+, p^+, μ_e, and ρ_e. (The subscript e denotes the edge of boundary layer.) Here $v^+ = v_n/u_\tau$, $p^+ = (dp/dx)(\nu/\rho u_\tau^3)$, and the friction velocity u_τ is given by $u_\tau = (\tau_w/\rho)^{1/2}$. The reader is referred to Ref. 15 for further details.

TLNS Procedure

The thin-layer Navier-Stokes equations written in general coordinates (ξ,η) are

$$\partial_t \hat{Q} + \partial_\xi \hat{E} + \partial_\eta \hat{F} = Re^{-1}\partial_\eta \hat{S} \tag{6}$$

The TLNS procedure (ARC2D) developed at NASA Ames Research Center[16] is adopted for this study. This implicit code is based on the Beam-Warming approximate-factorization algorithm. Euler implicit time-differencing and second-order central-spatial differencing are utilized. A nonlinear artificial dissipation model is added to capture nonoscillatory shock profiles and maintain stability. The diagonal version developed by Pulliam and Chaussee[17] is applied in the present study. Also, a space-varying time-step and a coarse- to fine-grid sequencing are used to accelerate the convergence rate.

On the airfoil surface, the normal wall velocity v_n is specified and the tangential velocity is set to zero. The pressure boundary condition at the airfoil surface is taken to be $\partial p/\partial\eta = 0$, since the η-coordinate lines are nearly orthogonal to the airfoil surface and the grids are very fine in the η direction near the airfoil surface. The adiabatic wall condition is used to obtain the density at the surface, and total energy is obtained from the equation of state. The far-field boundary conditions are obtained by imposing a compressible potential vortex solution on the free-stream quantities.[18] All the boundary conditions are updated explicitly in the TLNS procedure.

The Baldwin-Lomax turbulence model[19] used in the TLNS procedure is patterned after that of Cebeci-Smith, with modifications that make it unnecessary to find the outer edge of the boundary layer. However, the Baldwin-Lomax turbulence model did not consider blowing (or suction) effects on A^+, and the damping factor A^+ is redefined (from Ref. 20) as

$$A^+ = \frac{26}{(\tau^+)^n} \tag{7a}$$

In order to compare results with the STAN-5 results in Refs. 21 and 22 near the blowing (or suction) surface, the x-momentum equation is integrated with $v = v_w = \text{constant}$, $p_x/\rho = \text{constant}$, $\rho = \text{constant}$, and uu_x being neglected. The result is

$$\tau^+ \approx \tau_w^+ + p^+ y^+ + v^+ u^+ \tag{7b}$$

where τ^+, p^+, y^+, v^+, and u^+ are defined in the conventional way. Figure 2 shows plots of A^+ and p^+ with v^+ as a parameter. The symbols represent data from STAN-5.

It is observed from Fig. 2 that when $p^+ \approx -0.04$, and $v^+ = 0$, A^+ goes to ∞. For agreement with this, the denominator of Eq. (7a) should go to zero under those conditions:

$$\tau^+ = 1 - 0.04y^+ = 0$$

Thereby, $y^+ = 25$ is determined and extended to other cases, with $v^+ \neq 0$. The results from setting $y^+ = 25$ in Eq. (7b) and $n = 0.7$ in Eq. (7a) are shown as the solid lines in Fig. 2. It is seen that values of A^+ vs p^+ for various v^+ from this procedure agree well with the results from STAN-5. With this modification, the dependence of A^+ on boundary-layer edge quantities in the Cebeci-Smith turbulence model are avoided. Indeed, this value of n is in the range proposed by other researchers, such as Patankar and Spalding ($n = 0.5$)[23] and Baker et al.[24] ($n = 1.0$). The surface roughness also has a large effect upon A^+, but in the present work this is not considered.

This modification [Eq. (7a)] has been added to the Baldwin-Lomax turbulence model, yielding skin friction values in the blowing region higher than those calculated by the original Baldwin-Lomax model. Conversely, this model predicts skin friction in the suction region that is lower than that from the original model.[25] That is because in the modified version the blowing increases the mixing rate (A^+ being reduced), and the suction tends to laminarize the flow (A^+ being increased). These effects are neglected when an A^+ of 26 is assumed. Similarly, a strong adverse pressure gradient would reduce A^+ according to the modified version. The skin friction C_f/e for the RAE 2822, at $M_\infty = 0.73$, $C_L = 0.803$, and $Re = 6.5 \times 10^6$ with transition specified at 0.03 chord, is shown in Fig. 3. Results from the two models are compared with the computation of Mehta[26] and with experimental results by Cook et al.[27] All of the predictions agree well with experiment, but the modified turbulence model yields results that compare slightly better with experiment.

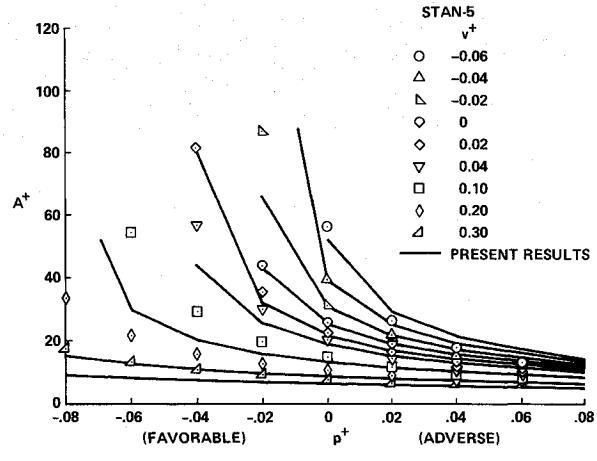

Fig. 2 Damping parameter A^+.

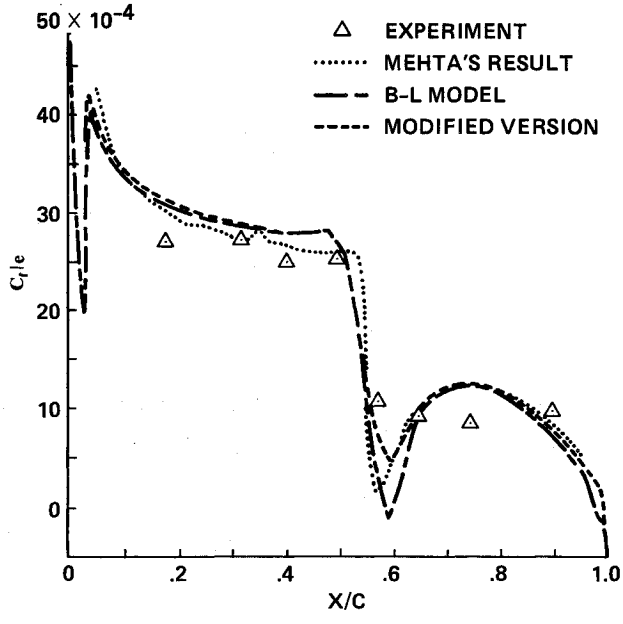

Fig. 3 Comparison of C_f/e distributions for an RAE 2822 airfoil at $M_\infty = 0.73$, $Re = 6.5 \times 10^6$, and $C_L = 0.803$.

Generally, the IBL procedure is at least one to two orders of magnitude faster than the TLNS procedure. For mildly separated transonic flow, it can provide very good results.[12,13] However, the range of allowable blowing rates is more restricted for the IBL procedure than for the TLNS approach. In addition, the steady first-order boundary-layer approximation becomes suspect when a strong shock and boundary-layer interaction occurs, because dp/dy in the boundary layer may not be negligible. At the expense of computing time, the TLNS procedure has fewer theoretical restrictions than the IBL procedure. Therefore, when a strong shock and boundary-layer interaction occurs or the transpiration velocity becomes large, the TLNS procedure is preferred.

Interface of Outer and Inner Flows

Since the holes in the porous region are very small and close together, it is difficult to compute the flow across the porous media without extremely fine grids. Therefore, in the present study the porosity effect is modeled instead of being computed. The model proposed is patterned after the treatment of porous wind tunnel walls based on Darcy's law.[28]

The transpiration velocity v_n for the outer flow is governed by Darcy's law, such that

$$v_n = -\frac{\bar{\sigma}}{\rho_\infty U_\infty}(p_{\text{outer}} - p_{\text{inner}}) \tag{8}$$

where the subscript outer indicates the outer-flow property and inner indicates the inner-flow property; $\bar{\sigma}$ is the porosity distribution function, which is determined by viscosity, as well as by the size and spacing of the holes in the porous surface. Two cavity models have been used in this work. Both models use mass conservation across the porous surface as a constraint to couple inner and outer flows. The first model that is considered assumes constant pressure in the cavity, as has been applied in Refs. 7-9. For the second model considered, the total pressure in the cavity is assumed to be constant. Also for simplicity, the flow in the cavity is assumed to be inviscid. The pressure variation in the cavity is obtained by solving the stream function formulation. The results obtained in Ref. 29 indicate the pressure variation is so negligible. Therefore, whether the first or the second model is used does not affect the outer solution. This might not be so for very thin cavities. However, the inviscid analysis for the cavity would become suspect for these geometries.

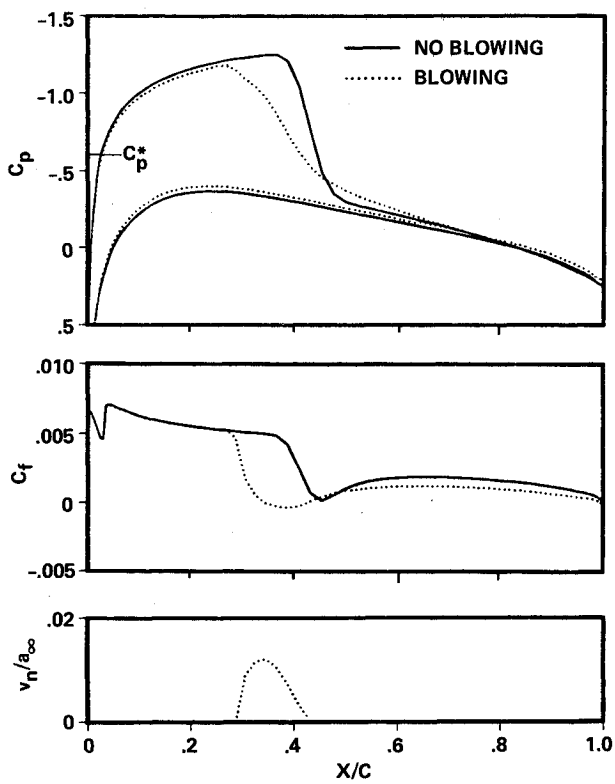

Fig. 4 Blowing ahead of the shock.

Grid Generation

In the IBL procedure, the C grid is generated by solving Poisson equations,[30] whereas the boundary-layer grid is a solution-adaptive grid, and the grid height in physical space is a function of computed displacement thickness. Grid points are clustered near the wall and wake centerline.[12] The inviscid grid size is 223×31, with additional 50 grid lines in the η direction for the boundary-layer algorithm. In the TLNS procedure, a C-type 251×65 grid is generated by solving hyperbolic equations.[31,32] Finally, a 431×10 grid in the cavity is generated algebraically.[25]

Numerical Results and Analysis

Effects of Active Blowing and Suction

Since the porous surface induces blowing in the supersonic region and suction in the subsonic region, it is meaningful to investigate separately the effects of blowing and suction on the shock and boundary-layer control.

The first test case utilizes a NACA 0012 airfoil at $M_\infty = 0.75$, and $\alpha = 2.0$ deg, the transition being specified at 0.03 chord, and $Re = 3.76 \times 10^6$. Generally, the numerical results show that blowing in the supersonic region weakens the shock and smoothes the pressure gradient. However, if the blowing is too strong, the results indicate that separation may occur in the blowing region and increase the thickness of the boundary layer approaching the trailing edge, which causes not only an increase in viscous pressure drag but also a large decambering effect leading to a decrease in lift.

For the case of blowing ahead of the shock, such as shown in Fig. 4, the results indicate that the pressure gradient is smoothed, C_D (pump drag being excluded) is reduced from 0.0191 to 0.0171, and C_L is also reduced from 0.3753 to 0.3059. Even though the blowing velocity in this case is less than 1.5% of the freestream velocity, separation is encountered in the blowing region. In other words, the drag reduction with normal blowing seems to be mainly a result of the weakened shock and the slight forward shift of the shock rather than the boundary-layer control achieved by increasing the mixing rate.

On the other hand, suction behind the shock generally increases the shock strength, moves the shock downstream, and delays separation. Shown in Fig. 5 is an example of these phenomena. In this case C_L is increased from 0.3753 to 0.4435, but C_L/C_D is improved only slightly because wave drag and skin-friction drag are also increased. Furthermore, the viscous pressure drag is not a dominant part of the total drag in this case, so the form-drag cannot be reduced significantly. The boundary-layer control aspect is shown by the fact that C_f is increased not only in the suction area, but also in the region downstream of the suction, indicating that suction probably allows a strong shock without separation or with controllable separation. Therefore, in regard to drag reduction, the above numerical results imply that the shock can be weakened by normal blowing and that boundary-layer control can be achieved by suction.

Porous Airfoils

It has been demonstrated in Refs. 12 and 13 that, except for slight differences near the shock and trailing edge, good agreement was found between the results obtained by using these IBL and TLNS procedures in solid-airfoil computations. Similarly, for a NACA 0012 airfoil at $M_\infty = 0.8$, $\alpha = 0.0$ deg, and $Re = 4.09 \times 10^6$, comparable C_D values of 0.0125 and 0.0123

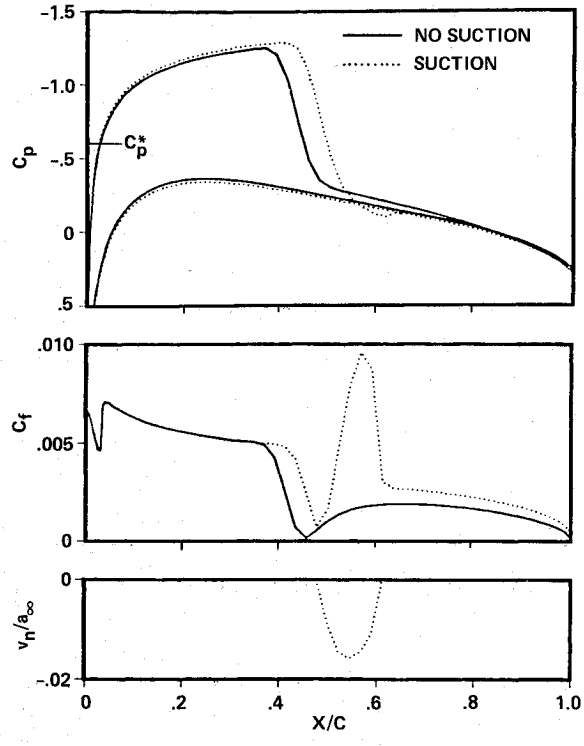

Fig. 5 Suction behind the shock.

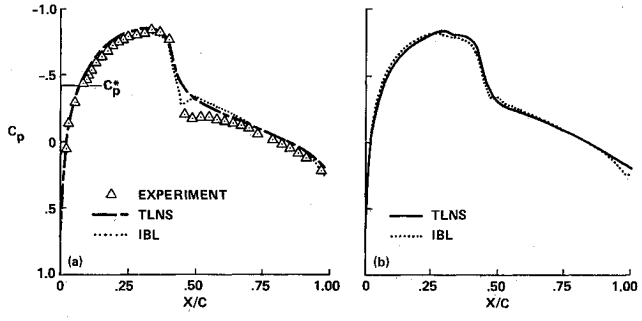

a) Computed and experimental results for a solid airfoil

b) Computed results for a porous airfoil

Fig. 6 Comparison of pressure distribution for an NACA 0012 airfoil: $M_\infty = 0.8$, $\alpha = 0$ deg, $Re = 4.09 \times 10^6$, $x_1 = 0.3$, $x_2 = 0.5$.

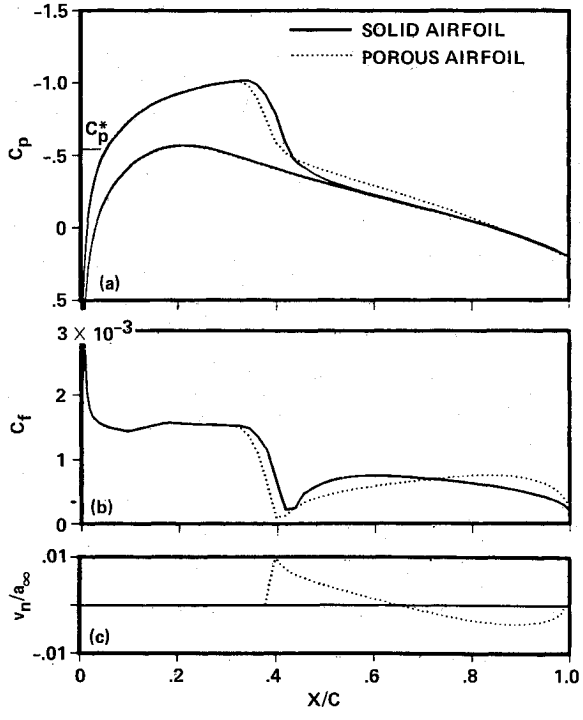

Fig. 7 Pressure, skin friction, and normal velocity distribution on a lifting NACA 0012 airfoil.

are obtained, respectively, with TLNS and IBL procedures. (From Ref. 33, the measured drag coefficient of the solid airfoil is 0.0106.)

Computed pressure distributions are plotted in Fig. 6a and shown with measured results. The same airfoil is then made porous with a porosity distribution $\bar{\sigma} = 0.1\ [\sin(x - x_1)\pi/(x_2 - x_1)]^{0.5}$ (the first cavity model) between $x_1 = 0.3$ and $x_2 = 0.5$ (on both upper and lower surfaces). The x_1 and x_2 parameters are the limits of the porous region. Again, comparable drag coefficients of 0.0127 (TLNS) and 0.0125 (IBL) are obtained numerically. Although Fig. 6b shows that the pressure jump is smeared by the porous surface, the pressure jump still has a tendency to move downstream. Since the airfoil surface over this region is backward facing, the lower pressure moving downstream would increase the pressure drag. The reduction in shock strength is not large enough to compensate for the increased viscous loss, so that the total drag of the porous airfoil becomes slightly higher than that of the solid airfoil. Such a phenomenon has also been observed in the laboratory at the lower M_∞ region,[1-4] but it has not been predicted by any inviscid-flow approach, which can only evaluate wave drag.[7-8]

For a lifting case, a calculation (based on the TLNS procedure) was made with a NACA 0012 airfoil at $M_\infty = 0.77$, with $\alpha = 1.0$ deg, with $Re = 4.09 \times 10^6$, with the transition fixed at 0.01 chords, and with the first cavity model having a porosity distribution $\bar{\sigma} = 0.07\ [\cos 0.5(x - x_s)\pi/(x_k - x_s)]^{0.5}$ (Ref. 8) that ranges from 0.378 to 1.000. (This distribution range covers a large portion of the upper surface.) The x_s parameter is the position of shock that would result if the porous surface was solid, and x_k represents either x_1 or x_2, depending on whether x is less or greater than x_s. It can be seen in Fig. 7 that the pressure jump across the shock is weakened, C_L is increased from 0.169 to 0.183, but again C_D is increased from 0.0125 to 0.0137 (C_L/C_D is slightly reduced), whereas the skin-friction drag is little changed. By comparison with the result for the solid airfoil, the skin friction is reduced in the blowing region and is increased in the suction region because of the porosity.

The numerical results presented in Figs. 8 and 10 (obtained with the TLNS procedure) are for a symmetrical airfoil that is generated by reflecting the upper surface of an RAE 2822 airfoil to the lower surface. The porous surfaces are from 0.615 to 0.805 (the second cavity model on both upper and lower surfaces) with a porosity $\bar{\sigma} = 0.4$. The bottom of the cavity is at $y/c = 0.0$. The flow and airfoil parameters are $Re = 6.5 \times 10^6$, $\alpha = 0.0$ deg, and the transition is fixed at 0.03. For the first case with $M_\infty = 0.82$ (Figs. 8 and 10), C_D is increased from 0.0258 to 0.0273 in the presence of the porous surface. The effects of the porosity are described as follows.

1) The comparison of C_p plots (Fig. 8) for the solid and porous airfoils shows that relative to the solid airfoil, the shock is weakened near the airfoil surface, and the pressure on the porous airfoil is lower at the trailing edge. The C_p plots also indicate that the original, one strong pressure jump becomes two consecutive weaker jumps, which represent the leading and rear legs of a lambda shock. In this case, the rear leg is slightly behind the original shock position on the solid airfoil. The lowered pressure at the trailing edge has also been observed experimentally by Raghunathan and Mabey,[4] who recently investigated the flow about a 6%-thick half-circular-arc model mounted on the upper wall of a wind tunnel (Fig. 9).

2) Blowing at the leading part of the porous region reduces C_f, and suction at the rear part of porous region makes the local C_f larger in the suction region, as shown in Fig. 10. But

downstream of the suction region, the flow has difficulty overcoming the adverse pressure gradient; as a result, the values of C_f are smaller than they are for the solid airfoil. Aft of the porous surface, separation occurs.

For the same airfoil, but at $M_\infty = 0.85$, the computed results indicate about a 10% reduction in drag ($C_D = 0.055$ for the solid airfoil, $C_D = 0.050$ for the porous airfoil.) The effects of porosity (Figs. 11–15) are described as follows.

1) The comparison of C_p plots (Fig. 11) again shows that relative to the solid airfoil, the shock is weakened near the airfoil surface and that the pressure on the porous airfoil is lower at the trailing edge. The C_p plots also indicate that the original, one strong pressure jump becomes two weaker jumps. However, the second pressure jump on the airfoil surface is moved upstream slightly, which is opposite to the finding in the previous case ($M_\infty = 0.82$ and C_D increased). The experimental results in Fig. 12 show the comparison of shock position between the solid and porous airfoils by Nagamatsu et al.[3] who studied a different supercritical airfoil. The experimental results may indicate that the drag is reduced when the downstream movement of the rear leg of the shock is retarded. From comparison with the last case (rear leg of shock moved downstream and drag was increased) and this case (rear leg of shock moved upstream and drag was reduced), there is a qualitative correlation between experiment and computation.

2) The separated region is enlarged on the porous airfoil (Figs. 13a and 13b) and the boundary layer becomes thicker. Figure 14b indicates that some of the fluid particles that are blown out are immediately sucked back into the cavity. But some of the fluid particles that are blown out at the upstream end of the porous surface enclose a dead air region before going back into the cavity.

According to the present numerical scheme and the turbulence and porosity modeling, for the passive shock and boundary-layer interaction at low angles of attack, there are two possible flow patterns above the porous surface (Fig. 14). There is a stagnation point in the flowfield of pattern 2 (Fig. 14b) that does not occur in pattern 1 (Fig. 14a). The

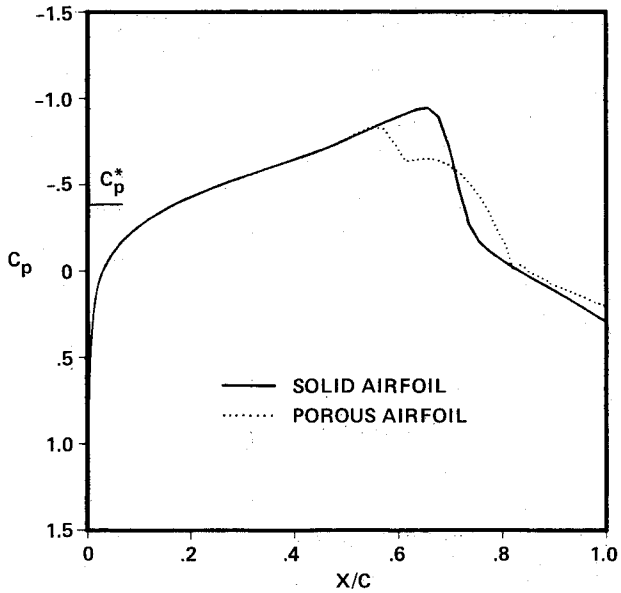

Fig. 8 Comparison of pressure distribution on the airfoil surface.

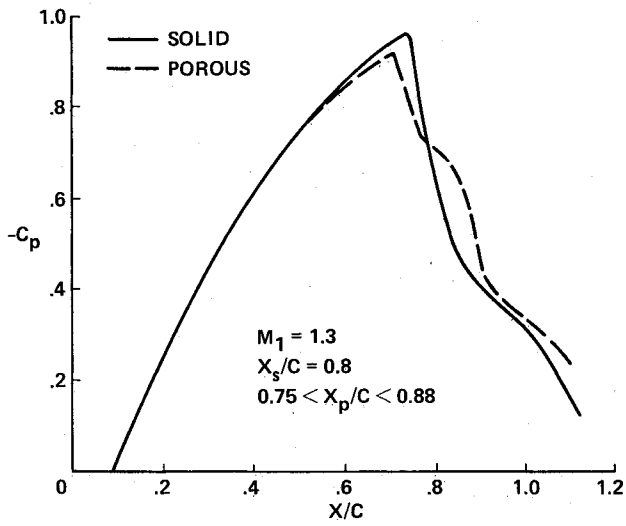

Fig. 9 Experimental pressure distribution of a 6%-thick half-circular-arc model.

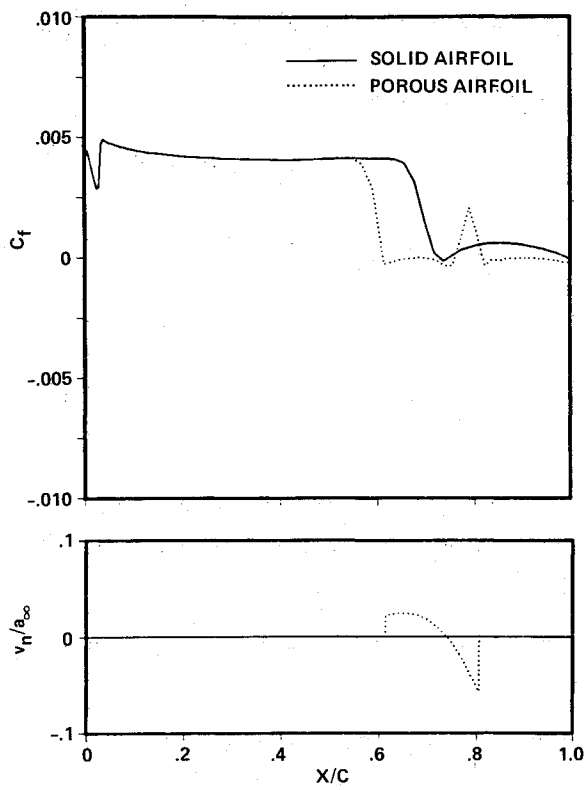

Fig. 10 Comparison of skin friction.

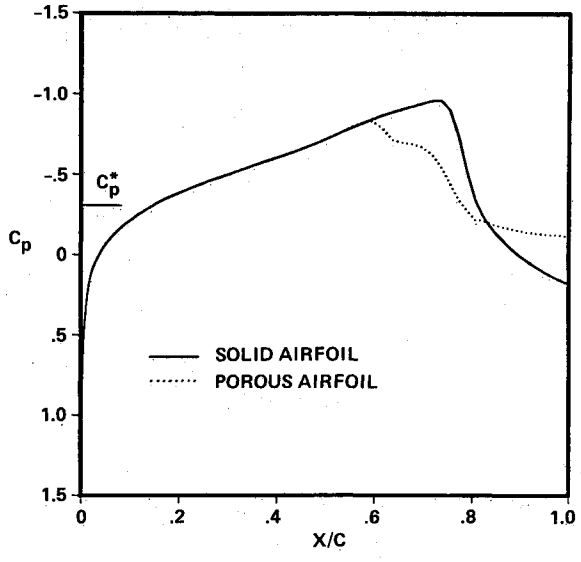

Fig. 11 Comparison of pressure distribution on the airfoil surface.

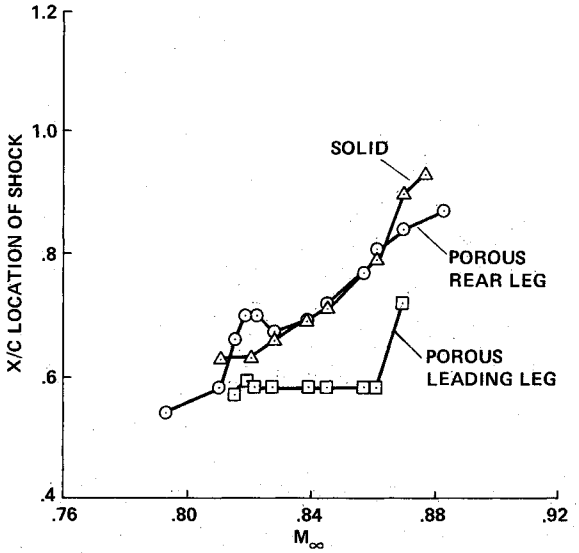

Fig. 12 Experimental results of shock movement on a supercritical airfoil.

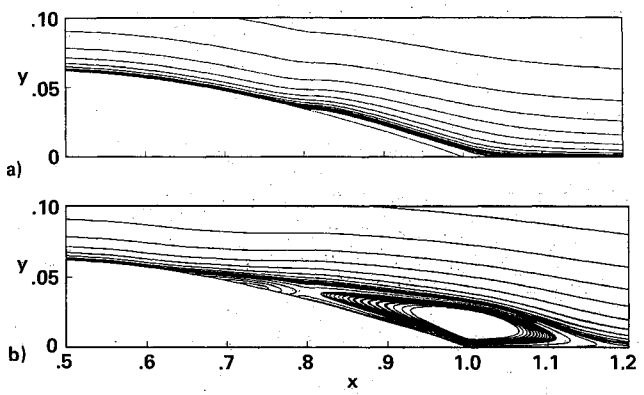

Fig. 13 Streamline patterns: a) solid airfoil; b) porous airfoil.

status of the flow in Figs. 8 and 11 is near a transition from pattern 1 to pattern 2, and the status of Fig. 14b is a typical pattern 2. Generally, when the shock is not strong, the top pattern occurs and the drag may not be reduced. When the shock becomes stronger, the bottom pattern may occur and the drag can be reduced. It can be expected that the separation bubble would burst intermittently and vortex shedding would occur when either Mach number or angle of attack is increased further, and that oscillations between patterns 1 and 2 would occur. Up until now, the only experimental investigations of the boundary layer near the porous region are those of Krogmann et al.[5] and Thiede et al.[6] The results of those experiments indicate that the boundary layer is thickened by using a perforated surface with a cavity. However, the present calculations of porosity effect on the boundary-layer control are still not as effective as experimental data show. The complete assessment would require the refined porosity and turbulence models. In addition, the computations of Olling and Dulikravich[9] indicate that the reduction of boundary-layer thickness could be possibly achieved with a nonconstant porosity distribution.

3) As shown in Fig. 15, the suction at the rear part of the porous region makes C_f more negative over the suction region, which is opposite to the effect shown in Fig. 10. This result is what would be expected, however, since the suction is trying to swallow the separation bubble that lies behind the suction region.

In summary, the results of the present nonlifting case reveal porosity effects at higher freestream Mach numbers: the shock becomes weaker, the shock is moved slightly upstream, and the viscous loss is increased. These findings are consistent with the

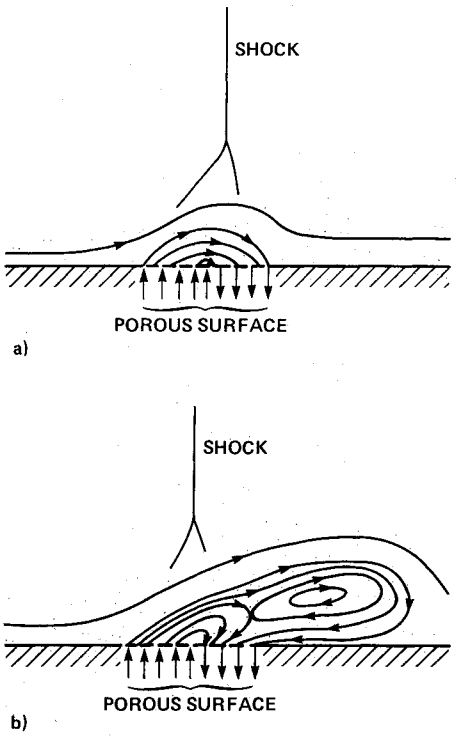

Fig. 14 Streamline pattern of passive shock and boundary-layer interaction. a) pattern 1; b) pattern 2.

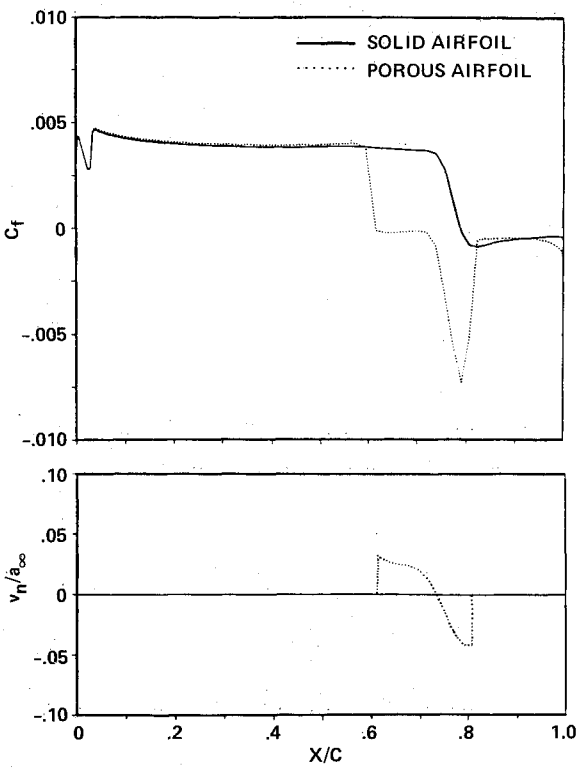

Fig. 15 Comparison of skin friction.

results of the last few cases, except here the reduction in shock strength is more than enough to compensate for the increased viscous loss. Also, the pattern-2 separated flow becomes mature, and movement of the shock downstream has been prevented. Boundary-layer separation occurs because of the blowing at the front part of the porous surface, and the suction at the rear part of the porous surface captures a dead air region.

The variation of C_D with increasing freestream Mach number for this airfoil with a slightly longer porous surface from

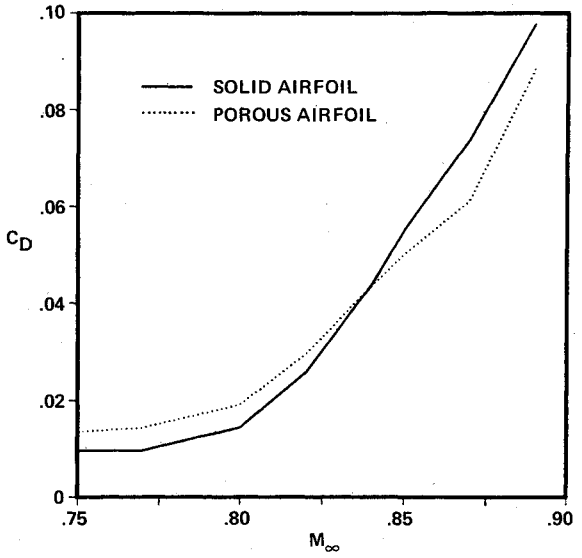

Fig. 16 Porosity effects on the drag of a modified RAE 2822 airfoil: $x_1 = 0.615$, $x_2 = 0.88$, $\bar{\sigma} = 0.4$, porosity on both upper and lower surfaces, the bottom of cavity at $y/c = 0.0$, $Re = 6.5 \times 10^6$, $\alpha = 0$ deg and transition fixed at 0.03.

0.615 to 0.88 is plotted in Fig. 16. Drag reduction by the porous surface occurs at Mach numbers higher than 0.84. Drag reductions of the same order of magnitude have been found experimentally by Nagamatsu et al.[3] in the study of a supercritical airfoil mounted on the bottom wall of a wind tunnel. Finally, the numerical results show that the total drag of the porous airfoil is reduced at higher Mach numbers and that it is increased at lower Mach numbers, as has been observed experimentally. However, the advantage of the highly limited suction area of the porous surface is not as effective as the experimental results would indicate.[3]

Concluding Remarks

A numerical study was made to examine the effects of a porous surface on transonic airfoil performance. The computational results qualitatively verify some available experimental data and improve the inviscid-flow solutions. The results obtained from constant porosity distribution can be used to predict the trend shown in the C_D vs M_∞, at $\alpha = 0$ deg. The results also show that the porous surface affects not only the shock strength and shock shape, but also the position of the shock. Furthermore, the structure of passive-shock and boundary-layer interactions and the streamline patterns near the porous surface are discussed.

Acknowledgments

The first two authors would like to acknowledge the support from NASA Ames Research Center through Grant NCC 2-355. The first author would like to thank B. Baldwin and C. M. Hung of NASA Ames Research Center for their invaluable suggestions and discussions during the course of this work. Special thanks to T. H. Pulliam for providing the ARC2D code.

References

[1]Bahi, L., Ross, J. M., and Nagamatsu, H. T., "Passive Shock Wave/Boundary Layer Control for Transonic Airfoil Drag Reduction," AIAA Paper 83-0137, Jan. 1983.

[2]Nagamatsu, H. T., Orozco, R. D., and Ling, D. C., "Porosity Effect on Supercritical Airfoil Drag Reduction by Shock Wave/Boundary Layer Control," AIAA Paper 84-1682, June 1984.

[3]Nagamatsu, H. T., Dyer, R., and Ficarra, R. V., "Supercritical Airfoil Drag Reduction by Passive Shock Wave/Boundary Layer Control in the Mach Number Range .75 to .90," AIAA Paper 85-0207, Jan. 1985.

[4]Raghunathan, S. and Mabey, D. G., "Passive Shock Wave Boundary Layer Control Experiments on a Circular Arc Model," AIAA Paper 86-0285, Jan. 1986.

[5]Krogmann, P., Stanewsky, E., and Thiede, P., "Effects of Suction on Shock/Boundary-Layer Interaction and Shock-Induced Separation," *Journal of Aircraft*, Vol. 22, Jan. 1985, pp. 37–42.

[6]Thiede, P., Krogmann, P., and Stanewsky, E., "Active and Passive Shock/Boundary-Layer Interaction Control on Supercritical Airfoils," *Improvement of Aerodynamic Performance through Boundary Layer Control*, AGARD CP-365, May 1984, pp. 24-1 to 24-13.

[7]Savu, G. and Trifu, O., "Porous Airfoils in Transonic Flow," *AIAA Journal*, Vol. 22, July 1984, pp. 989–991.

[8]Chen, C. L., Chow, C. Y., Holst, T. L., and Van Dalsem, W. R., "Numerical Simulation of Transonic Flow over Porous Airfoils," AIAA Paper 85-5022, Oct. 1985.

[9]Olling, C. R., and Dulikravich, G. S., "Porous Airfoil Analysis Using Viscous-Inviscid Coupling at Transonic Speeds," *International Journal for Numerical Methods in Fluids*, Vol. 7, Feb. 1987, pp. 103–129.

[10]Holst, T. L., "Implicit Algorithm for the Conservative Transonic Full-Potential Equation Using an Arbitrary Mesh," *AIAA Journal*, Vol. 17, Oct. 1979, pp. 1038–1045.

[11]Dougherty, F. C., Holst, T. L., Gundy, K. L., and Thomas, S. D., "TAIR—A Transonic Airfoil Analysis Computer Code," NASA TM-81296, 1981.

[12]Van Dalsem, W. R., "Simulation of Separated Transonic Airfoil Flow by Finite-Difference Viscous-Inviscid Interaction," Ph.D. Dissertation, Stanford University, Stanford, CA, June 1984.

[13]Van Dalsem, W. R. and Steger, J. L., "Finite-Difference Simulation of Transonic Separated Flow Using a Full-Potential Boundary-Layer Interaction Approach," AIAA Paper 83-1689, July 1983.

[14]Flores, J., Holst, T. L., Kwak, D., and Batiste, D. M., "New Consistent Spatial Differencing Scheme for the Transonic Full-Potential Equations," *AIAA Journal*, Vol. 22, No. 8, August 1984, pp. 1027-1034.

[15]Cebeci, T. and Smith, A. M. O., *Analysis of Turbulent Boundary Layers*, Academic, New York, 1974, pp. 213–221.

[16]Pulliam T. H., "Euler and Thin-Layer Navier-Stokes Codes," Notes for Computational Fluid Dynamics User's Workshop, The University of Tennessee Space Institute, Tullahoma, TN, Mar. 1984.

[17]Pulliam, T. H. and Chaussee, D. S., "A Diagonal Form of an Implicit Approximate-Factorization Algorithm," *Journal of Computational Physics*, Vol. 39, Feb. 1981, pp. 347–363.

[18]Salas, M., Jameson, A., and Melnik, R., "A Comparison Study of the Nonuniqueness Problem of the Potential Equation," AIAA Paper 83-1888, July 1983.

[19]Baldwin, B. S. and Lomax, H., "Thin-Layer Approximation and Algebraic Model for Separated Turbulent Flows," AIAA Paper 78-257, 1978.

[20]Bushnell, D. M., Cary, A. M., Jr., and Harris, J. E., "Calculation Methods for Compressible Turbulent Boundary Layers—1976," NASA SP-422, 1977.

[21]Crawford, M. E. and Kays, W. M., "STAN-5—A Program for Numerical Computation of Two-Dimensional Internal and External Boundary Layer Flows," NASA CR-2742, 1976.

[22]Kays, W. M. and Moffat, R. J., "The Behavior of Transpired Turbulent Boundary Layers," NASA CR-119147, 1985.

[23]Patankar, S. V. and Spalding, D. B., *Heat and Mass Transfer in Boundary Layers*, 2nd ed., International Textbook Co., London, 1970.

[24]Baker, R. J., Jonsson, V. K., and Launder, B. E., "The Turbulent Boundary Layer with Streamwise Pressure Gradient and Foreign-Gas Injection," Imperial College Report ET/TN/G/31, London.

[25]Chen, C. L., "Computation of Transonic Flow over Porous Airfoils," Ph.D. Dissertation, University of Colorado, Boulder, CO, Aug. 1986.

[26]Mehta, U., "Reynolds-Averaged Navier-Stokes Computations of Transonic Flows around Airfoils," Presented at the Second Symposium on Aerodynamic Flow, Long Beach, CA, Jan. 1983.

[27]Cook, P. H., McDonald, M. A., and Firmin, M. C. P., "Aerofoil RAE 2822—Pressure Distributions and Boundary Layer and Wake Measurements," AGARD AR 138, Paper A6, 1979.

[28]Baldwin, B. S. and Turner, J. B., "Wall Interference in Wind Tunnels With Slotted and Porous Boundaries at Subsonic Speeds," NACA TN-3176, 1953.

[29]Chen, C. L., Chow, C. Y., Van Dalsem, W. R., and Holst, T. L., "Computation of Viscous Transonic Flow over Porous Airfoils," AIAA Paper 87-0359, Jan. 12–15, 1987.

[30]Sorenson, R. L., "A Computer Program to Generate Two-Dimensional Grids about Airfoils and Other Shapes by the Use of Poisson's Equation," NASA TM-81198, 1980.
[31]Steger, J. L. and Chaussee, D. S., "Generation of Body-Fitted Coordinates Using Hyperbolic Partial Differential Equations," Report 80-1, Sunnyvale, CA, Flow Simulations, Inc., Jan. 1980.
[32]Barth, T. J., Pulliam, T. H., and Buning, P. G., "Navier-Stokes Computations for Exotic Airfoils," AIAA Paper 85-0109, Jan. 1985.
[33]Thibert, J. J., Grandjacques, M., and Ohman, L. H., "NACA 0012 Airfoil," AGARD AR 138, Paper A1, 1979.